Optimal Central Frequency for Non-Contact Vital Sign Detection Using Monocycle UWB Radar

Artit Rittiplang [1], Pattarapong Phasukkit [1,*] and Teerapong Orankitanun [2]

[1] Faculty of Engineering, King Mongkut's Institute of Technology Ladkrabang, Bangkok 10520, Thailand; 59601306@kmitl.ac.th

[2] Engineering Department, Royal Thai Naval Academy, Samutprakarn 10270, Thailand; teerapong.o@navy.mi.th

* Correspondence: pattarapong.ph@kmitl.ac.th

Abstract: Ultra-wideband (UWB) radar has become a critical remote-sensing tool for non-contact vital sign detection such as emergency rescues, securities, and biomedicines. Theoretically, the magnitude of the received reflected signal is dependent on the central frequency of mono-pulse waveform used as the transmitted signal. The research is based on the hypothesis that the stronger the received reflected signals, the greater the detectability of life signals. In this paper, we derive a new formula to compute the optimal central frequency to obtain as maximum received reflect signal as possible over the frequency up to the lower range of Ka-band. The proposed formula can be applicable in the optimization of hardware for UWB life detection and non-contact monitoring of vital signs. Furthermore, the vital sign detection results obtained by the UWB radar over a range of central frequency have been compared to those of the former continuous (CW) radar to provide additional information regarding the advantages and disadvantages of each radar.

1. Introduction

Nowadays, radars not only are used to detect long-ranged targets such as military airplanes, but also they are used for short-range detections, especially in the monitoring of human activities, monitoring sleeping infants or adults, etc. In such biomedical applications, radars can be widely categorized into types, namely continuous wave (CW) radar and ultra-wideband (UWB) radar. Each of these radars has its own advantages and disadvantages as follows.

CW radars can provide accurate Doppler frequency measurements. They are of compact size, have low cost, longer detection range, and robust operation for practical portable and handheld applications. Therefore, CW radars are popular monitoring tools of human health such as sleep apnea syndrome, breathing disorder detection, and non-contact monitoring of the respiration of patients in hospitals [1–11].

UWB radars emit low electromagnetic radiation and, thus, consume relatively low levels of power. This is because UWB pulse duration is typically in the order of nanoseconds. UWB radars can provide high precision in target ranging up to centimeter scale, and have more penetrating capabilities through obstacles compared with CW radars. Nowadays, UWB radars are popularly used for detecting multiple targets through walls, finding individuals buried underneath earthquake rubble, breast cancer monitoring, medical microwave imaging, and non-contact vital sign detection [12–39].

Due to the distance between the target and the radar, a stronger received signal is strictly required to overcome noises and interferences, especially for tiny vital motions such as breathing and heartbeat

motions. For UWB radars, the strengths of the heartbeat and breathing signals can be improved by adjusting the central frequency of the mono-pulse transmitted waveform. For CW radar, the carrier frequency of CW radars can be increased up to the lower region of the Ka-band to improve detection accuracy, because the short wavelength of the Ka-band sensor is capable of detecting small movements like chest-wall motion [7,8]. In practice, we do not have the luxury of unlimited bandwidth for which we can sweep across the entire range of frequencies. This is because the remote-sensing hardware (like antennas, PA, LNA), once set up, can operate at best on a few gigahertz of bandwidth. This practical problem has become our motivation to investigate the optimal central frequency for non-contact vital sign detection using a monocycle UWB radar. The organization of this paper is as follows.

The theoretical background is presented in Section 2. Then, in Section 3, a new model is derived from approximation techniques to theoretically investigate the optimal frequency, key parameters, behaviors and recovering vital sign spectra. The formula to obtain the optimal central frequency is derived from the new model into the simple formula. The simulations and experiments are presented in Sections 4 and 5, respectively. As an extra study, in Section 4.4, the central frequency of the UWB radar has been compared to the carrier frequency of CW radar to provide additional information regarding the advantages and disadvantages of non-contact vital sign detection.

2. Background

2.1. Transmitted Signal Model

In impulse radio ultra-wideband (IR-UWB) radar applications, one of the most simple-to-generate transmitting pulses is monocycle waveform, as illustrated in Figure 1a. The waveform defined as the first derivative of the Gaussian pulse can be easily generated by microwave circuits or FPGA boards with low distortion [14–25]. In time domain, the amplitude, $s(t)$, of the monocycle waveform is defined as [20–22]

$$s(t) = -\frac{2\sqrt{e}}{t_d} A_0 t e^{-2\left(\frac{t}{t_d}\right)^2} \tag{1}$$

where $t_d = 1/(\pi k_c)$ is the time duration between the maximum and minimum, k_c is the central frequency (Hz), and A_0 is the transmitting amplitude. The maximum and minimum values of $s(t)$ are, respectively, A_0 and $-A_0$ due to the multiplication factor $-2\sqrt{e}/t_d$.
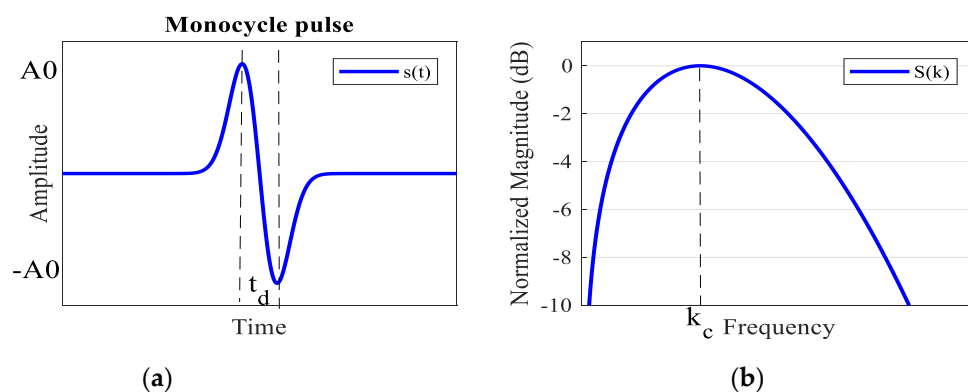
Figure 1. The 1st order Gaussian function: (**a**) time domain (**b**) frequency domain.

In the frequency domain, the monocycle wave form of (1) can be obtained by applying the Fourier transform (note that $tf(t) \leftrightarrow (j/2\pi)(dF(k)/dk)$)

$$S(k) = \int_{-\infty}^{\infty} s(t) e^{-j2\pi kt} dt = -\frac{2\sqrt{e}}{t_d} A_0 \int_{-\infty}^{\infty} t e^{-2\left(\frac{t}{t_d}\right)^2} e^{-j2\pi kt} dt = s_0 k e^{-\alpha k^2} \tag{2}$$

where

$$s_0 = j\frac{A_0}{k_c^2}\sqrt{\frac{e}{2\pi}} \quad \text{and} \quad \alpha = \frac{1}{2k_c^2} \tag{3}$$

The frequency domain of the transmitting signal is plotted in Figure 1b. From (2) and (3), the 3db-bandwidth of the transmitting signal $s(t)$ depends on the central frequency k_c as well as the order of the Gaussian pulse [20].

2.2. Received Signal Model

In general, the received signal can be modeled as the summation of multipath reflected signals from different objects with time delay, that is

$$R(t,\tau) = \sum_p \sigma_p s\left(t - t_p\right) + \sum_o \sigma_o s(t - t_o(\tau)) + \sum_v \sigma_v s(t - t_v(\tau)) \tag{4}$$

The first term represents the multipath signals reflected from stationary objects with reflection coefficient (σ_p) and time delay (t_p). Also, the second term also represents the multipath signals reflected from non-stationary objects with reflection coefficient (σ_o) and time delay (t_o). Lastly, the third term is the multipath signals reflected from human vital signs with reflection coefficient (σ_v) and time delay (t_v). From (4), $R(t,\tau)$ is a function of "fast time" t, which is the wave-propagation time, and "slow time" τ, which is the time of signal detection.

For this research, the analysis focused on vital sign motion of one human. Therefore, the received signal in (4) can be reduced to

$$R(t,\tau) = \sigma_v s(t - t_v(\tau)) \tag{5}$$

where the delay time $t_v(\tau)$ is equal to $2d(\tau)/c$ (c is the speed of light in vacuum). The distance to the target is

$$d(\tau) = d_0 + m_h \sin(2\pi f_h \tau) + m_r \sin(2\pi f_r \tau) \tag{6}$$

where d_0 is the nominal distance between the radar and the human chest. The m_h and m_r are, respectively, the movement amplitudes of the heart and respiration. The f_h and f_r are, respectively, the fundamental frequencies corresponding to heartbeat and respiration. From (6), the time delay in (5) can be written as

$$t_v(\tau) = 2d(\tau)/c = t_0 + t_h \sin(2\pi f_h \tau) + t_r \sin(2\pi f_r \tau) \tag{7}$$

where t_0, t_r, and t_h are the delays related to the human distance, respiratory and heart motions, respectively.

2.3. Detection Block Diagram

A block diagram of the radar system and received signal in both fast and slow times are shown in Figure 2a,b, respectively. The principle of detecting physiological movements is based on the phase shift of the received reflected signals in the slow-time domain. The signals from stationary objects do not shift in the slow-time domain. The human chest exhibits periodic movement, as shown by (6) and (7), and will induce the shift of the signal along the slow-time domain. From [22–39], the vital sign spectrum $Y(t_0,f)$ is defined as the Fourier transform of the received signal in its slow-time domain that is

$$Y(t_0, f) = \sigma_v \sum_{u=-\infty}^{\infty} \sum_{l=-\infty}^{\infty} C_{lu}(t_0)\delta(f - lf_h - uf_r) \tag{8}$$

where

$$C_{lu}(t_0) = \int_{-\infty}^{\infty} J_l\left(\frac{4\pi m_h}{\lambda}\right)J_u\left(\frac{4\pi m_r}{\lambda}\right)S(k)dk \tag{9}$$

defined as the spectral coefficient of the *l*-th harmonic of the heartbeat and the *u*-th harmonic of respiration. In (8), the $\delta(.)$ is a Dirac delta function. In (9), J_l and J_u are Bessel functions of the first kind for heartbeat and respiration, respectively. The $S(k)$ is defined in (2) and λ is the wavelength associated with the central frequency of transmitted wave. From (9), it is seen that the spectral coefficient C_{lu} is dependent on both the central frequency (through λ) of the signal and the movement amplitude, m_r and m_h. The coefficient C_{lu} not only is related to the harmonics of respiration and heartbeat signals, but also related the intermodulation effects between them as well [8].
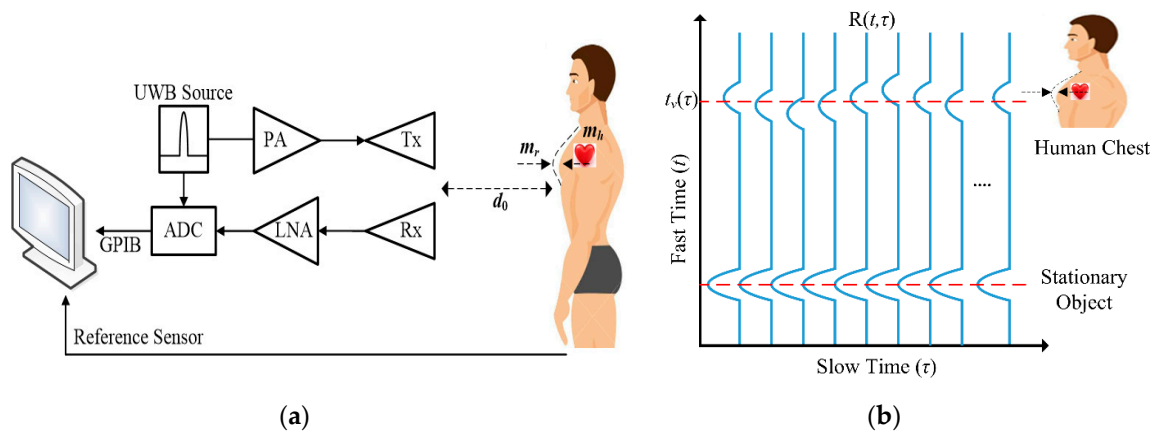
Figure 2. (**a**) A simplified block diagram of the radar system; (**b**) Rx signal depends on the chest movement.

3. Spectral Coefficient Solution

In this section, the spectral coefficients C_{lu} in (9) will be simplified using an approximation technique. Then the formula of the optimal central frequency will be derived by taking the derivative of the magnitude of the received signal with respect to the central frequency of the transmitted signal. The optimization criteria aim to maximize the magnitude of the received signal.

In general, the heart movement is usually less than 0.3 mm [40]. For frequencies up to 40 GHz, the Bessel functions J_l in (9) can be approximated [7], that is

$$J_l\left(\frac{4\pi m_h}{\lambda}\right) \approx \frac{1}{l!}\left(\frac{2\pi m_h}{\lambda}\right)^l \tag{10}$$

Figure 3 shows the comparison between the original Bessel function of the first kind and its linear approximation for (a) heartbeat, and (b) respiration. However, for respiration, the movement amplitude m_r is large compared to the wavelength λ. The approximation does not provide good accuracy, as shown in Figure 3b. For the respiration case, we use

$$J_u\left(\frac{4\pi m_r}{\lambda}\right) = \sum_{p=0}^{\infty} \frac{(-1)^p (2\pi m_r/\lambda)^{u+2p}}{p!(u+p)!} \tag{11}$$

Next, by substituting (2), (10) and (11) into (9) and letting $\lambda = c/k$, we have

$$C_{lu}(t_0) = \frac{s_0}{l!}\left(\frac{2\pi m_h}{c}\right)^l \sum_{p=0}^{\infty} \frac{(-1)^p (2\pi m_r/c)^{u+2p}}{p!(u+p)!} \int_{-\infty}^{\infty} k^{u+l+2p+1} e^{-\alpha k^2} dk \tag{12}$$
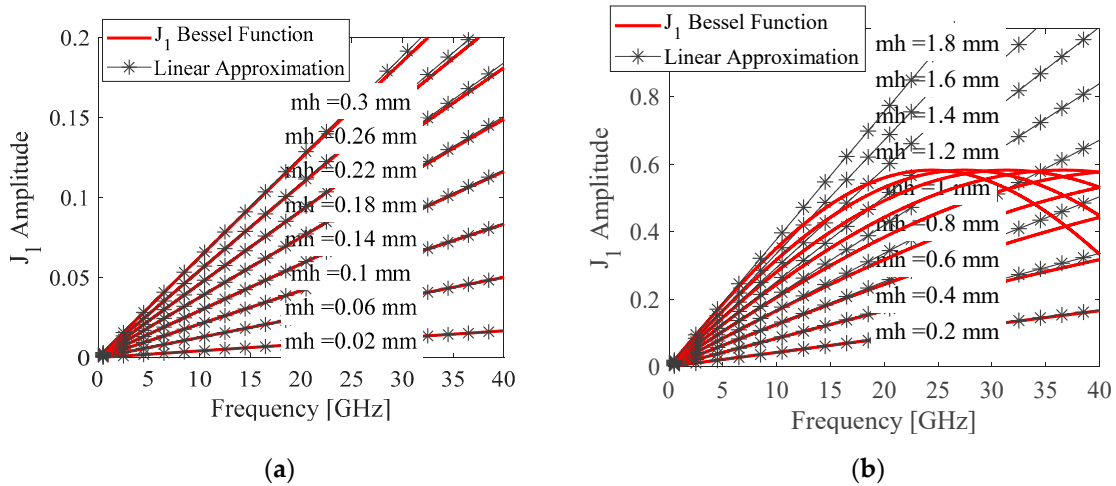
Figure 3. Comparison between the Bessel function of the first kind of order 1 and the linear approximation for the movement amplitude cases of (**a**) heartbeat; (**b**) respiration.

The integral term of the above equation can be evaluated by applying the Gaussian integral of general order [41], that is

$$
C_{lu}(t_0) = \begin{cases} \dfrac{s_0}{l!}\left(\dfrac{2\pi m_h}{c}\right)^l \sum_{p=0}^{\infty} \dfrac{(-1)^p \left(\frac{2\pi m_r}{c}\right)^{u+2p}}{p!(u+p)!} \sqrt{\dfrac{\pi}{\alpha}}\dfrac{(n-1)!!}{(2\alpha)^{\frac{n}{2}}} & ; \quad \text{for } n = u+l+2p+1 = \text{even} \\[3mm] 0 & ; \quad \text{for } n = u+l+2p+1 = \text{odd} \end{cases} \tag{13}
$$

By letting α and s_0 as in (3) and $k_c = c/\lambda_c$, we have

$$
C_{lu}(t_0) = \frac{jA_0\sqrt{e}}{l!}\left(\frac{2\pi m_h}{\lambda_c}\right)^l \sum_{p=0}^{\infty} \frac{(-1)^p (2\pi m_r/\lambda_c)^{u+2p}}{p!(u+p)!}(u+l+2p)!! \tag{14}
$$

The power series term above can be viewed as the Bessel function of (11) multiplied by the double factorial term $(u + l + 2p)!!$ Thus, we define

$$
G_{lu}\left(\frac{4\pi m_r}{\lambda_c}\right) = \sum_{p=0}^{\infty} \frac{(-1)^p (2\pi m_r/\lambda_c)^{u+2p}}{p!(u+p)!}(u+l+2p)!! \tag{15}
$$

where $(u + l + 2p)!! = (u + l + 2p)!/[2^{(u+l+2p-1)/2} \cdot ((u + l + 2p - 1)/2)!]$, the above function depends on $4\pi m_r/\lambda_c$ with l and u orders, and it is convergent by the well-known ratio test

$$
\lim_{p\to\infty}\left|\frac{a_{p+1}}{a_p}\right| = \lim_{p\to\infty}\frac{(u+l+2p)(2\pi m_r/\lambda_c)^2}{(p+1)(u+p+1)} = 0 \tag{16}
$$

Consequently, (14) can be rewritten as

$$
C_{lu}(\lambda_c, m_r, m_h) = \begin{cases} \dfrac{jA_0\sqrt{e}}{l!}\left(\dfrac{2\pi m_h}{\lambda_c}\right)^l G_{lu}\left(\dfrac{4\pi m_r}{\lambda_c}\right) & , \quad u+l = \text{odd} \\[3mm] 0 & , \quad u+l = \text{even} \end{cases} \tag{17}
$$

From the above equation, we can initially observe that for given values of m_r and m_h, the coefficient C_{lu} (the received signal strength) can be improved by increasing the central frequency ($k_c = c/\lambda_c$). Note also that the −3 db bandwidth is dependent on the central frequency as well as the type of

Gaussian pulse defining the transmitting signal [20]. In the next section, the optimal central frequencies for both respiratory and heartbeat models will be derived.

3.1. Respiratory Model

The harmonic components of the respiratory can be obtained by letting $l = 0$ [25], in (17) that is

$$C_{0u}(\lambda_c, m_r) = \begin{cases} jA_0 \sqrt{e}G_{0u}\left(\frac{4\pi m_r}{\lambda_c}\right) & , \quad u = \text{odd} \\ 0 & , \quad u = \text{even} \end{cases} \tag{18}$$

The spectral coefficient decays as the order number of u increases. From [25–27], the harmonic orders of $u = 0, 1, 2$ and 3 are significant for respiration spectrum, and we can evaluate them as

$$\begin{aligned} C_{00}(\lambda_c, m_r) &= C_{02}(\lambda_c, m_r) = 0 \\ C_{01}(\lambda_c, m_r) &= jA_0 \sqrt{e}G_{01}\left(\frac{4\pi m_r}{\lambda_c}\right) \\ C_{03}(\lambda_c, m_r) &= jA_0 \sqrt{e}G_{03}\left(\frac{4\pi m_r}{\lambda_c}\right) \end{aligned} \tag{19}$$

By substituting (19) into (8), we have

$$Y_{resp}(t_0, f) = \sigma_v \sum_{u=0}^{3} C_{0u}(\lambda_c, m_r)\delta(f - uf_r) = R_1\delta(f - f_r) + R_3\delta(f - 3f_r) \tag{20}$$

where R_1 is the coefficient of the fundamental frequency f_r. R_3 is the coefficient of the third harmonic $3f_r$. These quantities R_1 and R_3 can be evaluated as

$$R_1 = j\sigma_v A_0 \sqrt{e}G_{01}\left(\frac{4\pi m_r}{\lambda_c}\right) \quad \text{and} \quad R_3 = j\sigma_v A_0 \sqrt{e}G_{03}\left(\frac{4\pi m_r}{\lambda_c}\right) \tag{21}$$

Note that the R_3 should be minimized as possible, since it could interfere with the detectability of the fundamental frequency of the heartbeat signal. This is because, while their spectra are very close, the amplitude of R_3, which is relatively large, could superimpose on the heartbeat signal [25]. To improve the detectability of the fundamental respiration frequency, the optimal frequency can be obtained by taking the derivative of the above equation with respect to central frequency, that is

$$\frac{\partial R_1}{\partial k_c} = \frac{\partial G_{01}(4\pi m_r/\lambda_c)}{\partial k_c} = 0 \tag{22}$$

G_{01} was computed from (15) power-series expansion, thus we have

$$\sum_{p=0}^{\infty} \frac{(-1)^p (2p+1)(2p+1)!!}{p!(p+1)!}\left(\frac{2\pi m_r}{\lambda_c}\right)^{2p} = 0 \tag{23}$$

$$\begin{aligned} &1 - \frac{3(3)!!}{1!2!}\left(\frac{2\pi m_r}{\lambda_c}\right)^2 + \frac{5(5)!!}{2!3!}\left(\frac{2\pi m_r}{\lambda_c}\right)^4 - \frac{7(7)!!}{3!4!}\left(\frac{2\pi m_r}{\lambda_c}\right)^6 + \frac{9(9)!!}{4!5!}\left(\frac{2\pi m_r}{\lambda_c}\right)^8 \\ &- \frac{11(11)!!}{5!6!}\left(\frac{2\pi m_r}{\lambda_c}\right)^{10} + \frac{13(13)!!}{6!7!}\left(\frac{2\pi m_r}{\lambda_c}\right)^{12} - \frac{15(15)!!}{7!8!}\left(\frac{2\pi m_r}{\lambda_c}\right)^{14} + \ldots = 0 \end{aligned} \tag{24}$$

The high-order polynomial cannot easily be factored, we need to use numerical techniques to find a polynomial's roots. With the polynomial roots command in MATLAB program and for-loop coding, we discovered that $2\pi m_r/\lambda_c = 0.597$ is the valid root corresponding to the global maximum of the function. Finally, the optimal central frequency (k_{OR1}) to maximize the respiration strength can be derived as

$$k_{OR1} = 0.597\frac{c}{2\pi m_r} \tag{25}$$

which is inversely proportional to the respiratory movement amplitude m_r. In practice, for a fixed or approximated value of m_r, the corresponding optimal central frequency of the transmitted signal can be easily calculated by using (25).

3.2. Heartbeat Model

Similar to the respiration case, the harmonics of the heartbeat can be obtained by substituting index $u = 0$ into (17). We have

$$C_{l0}(\lambda_c, m_r, m_h) = \begin{cases} \frac{jA_0\sqrt{e}}{l!}\left(\frac{2\pi m_h}{\lambda_c}\right)^l G_{l0}\left(\frac{4\pi m_r}{\lambda_c}\right) & , \quad l = \text{odd} \\ \\ 0 & , \quad l = \text{even} \end{cases} \tag{26}$$

It is seen from the above equation that C_{l0} is dependent on k_c, m_h and especially m_r. This is because the chest motion m_r also affects the heartbeat movement [8,24,25], The dominant spectra of the heartbeat signal are

$$Y_{heart}(t_0, f) = \sigma_v \sum_{l=0}^{3} C_{l0}(\lambda_c, m_r, m_h)\delta(f - lf_h) = H_1\delta(f - f_h) + H_3\delta(f - 3f_h) \tag{27}$$

where H_1 is the coefficient of the fundamental frequency and H_3 is the coefficient of the third harmonic of heartbeat, which can be written as

$$H_1 = j\sigma_v A_0\sqrt{e}\left(\frac{2\pi m_h}{\lambda_c}\right)G_{10}\left(\frac{4\pi m_r}{\lambda_c}\right) \quad \text{and} \quad H_3 = j\sigma_v A_0\sqrt{e}\frac{1}{6}\left(\frac{2\pi m_h}{\lambda_c}\right)^3 G_{30}\left(\frac{4\pi m_r}{\lambda_c}\right) \tag{28}$$

The heartbeat estimation observed from the fundamental frequency can be erroneous; consequently, we can better detect that by maximizing its strength with the optimal frequency. We take the maximum derivative with respect to k_c, that is

$$\frac{\partial H_1}{\partial k_c} = \frac{\partial\left\{\left(\frac{2\pi m_h}{\lambda_c}\right)G_{10}\left(\frac{4\pi m_r}{\lambda_c}\right)\right\}}{\partial k_c} = 0 \tag{29}$$

and apply the product rule

$$\left(\frac{2\pi m_h}{\lambda_c}\right)\frac{\partial G_{10}\left(\frac{4\pi m_r}{\lambda_c}\right)}{\partial k_c} + G_{10}\left(\frac{4\pi m_r}{\lambda_c}\right)\frac{\partial\left(\frac{2\pi m_h}{\lambda_c}\right)}{\partial k_c} = 0 \tag{30}$$

Then, substituting (15) for $G_{10}(4\pi m_r/\lambda_c)$ to the above equation yields

$$\sum_{p=0}^{\infty} \frac{(-1)^p(2p+1)(2p+1)!!}{(p!)^2}\left(\frac{2\pi m_r}{\lambda_c}\right)^{2p} = 0 \tag{31}$$

$$1 - \frac{3(3)!!}{(1!)^2}\left(\frac{2\pi m_r}{\lambda_c}\right)^2 + \frac{5(5)!!}{(2!)^2}\left(\frac{2\pi m_r}{\lambda_c}\right)^4 - \frac{7(7)!!}{(3!)^2}\left(\frac{2\pi m_r}{\lambda_c}\right)^6 + \frac{9(9)!!}{(4!)^2}\left(\frac{2\pi m_r}{\lambda_c}\right)^8 \\ - \frac{11(11)!!}{(5!)^2}\left(\frac{2\pi m_r}{\lambda_c}\right)^{10} + \frac{13(13)!!}{(6!)^2}\left(\frac{2\pi m_r}{\lambda_c}\right)^{12} - \frac{15(15)!!}{(7!)^2}\left(\frac{2\pi m_r}{\lambda_c}\right)^{14} + \ldots = 0 \tag{32}$$

The valid root for maximization is $2\pi m_r/\lambda_c = 0.3901$ with the same method as (24), then the optimal central frequency (k_{OH1}) to maximize the heartbeat strength H_1 is

$$k_{OH1} = 0.3901\frac{c}{2\pi m_r} \tag{33}$$

From the above equation, k_{OH1} is inversely proportional to m_r. It is very important to note that although the H_1 value can be maximized via the optimal central frequency as in (33), the undesired third respiratory harmonic (R_3) begins to increase as the frequency increases, and R_3 degrades the detection accuracy of the heartbeat signal. Hence, the optimal central frequency for increasing H_1 strength should not give rise to R_3. The relevant discussion is provided in Section 4.2.

3.3. Avoiding the Central Frequency for the Peak R_3 harmonic and the Null Point H_1

As mentioned before, the third respiratory harmonic, R_3 will degrade the accuracy of detection and its value increases as the frequency increases. The constraint should put the range of frequency at which the radar operates to avoid the occurrence of the third harmonic, especially its peak value. Similar to the R_1 case, the frequency at the maximum R_3 can be obtained via derivatives,

$$k_{avoid,R3} = 1.1405 \frac{c}{2\pi m_r} \tag{34}$$

Also, it is worth pointing out that there is one frequency at which $H_1 = 0$. This is defined as the null point $k_{null,\,H1}$, which can be obtained by solving

$$H_1 = \left(\frac{2\pi m_h}{\lambda_c}\right) G_{10}\left(\frac{4\pi m_r}{\lambda_c}\right) = 0 \tag{35}$$

the null frequency can be obtained as

$$k_{null,H1} = 0.9533 \frac{c}{2\pi m_r} \tag{36}$$

On the contrary, the R_1 strength has no null-point, which will be discussed in Section 4.1.

3.4. Vital Sign Spectrum Model of Monocycle UWB

According to (20) and (27), the vital sign signal model in (8) can be rewritten as

$$Y(t_0, f) = j\sigma_v A_0 \sqrt{e}\overbrace{\left[G_{01}\left(\frac{4\pi m_r}{\lambda_c}\right)\delta(f - f_r) + G_{03}\left(\frac{4\pi m_r}{\lambda_c}\right)\delta(f - 3f_r)\right.}^{Y_{resp}(t_0,f)}$$
$$\underbrace{\left. + \left(\frac{2\pi m_h}{\lambda_c}\right)G_{10}\left(\frac{4\pi m_r}{\lambda_c}\right)\delta(f - f_h) + \frac{1}{6}\left(\frac{2\pi m_h}{\lambda_c}\right)^3 G_{30}\left(\frac{4\pi m_r}{\lambda_c}\right)\delta(f - 3f_h)\right]}_{Y_{heart}(t_0,f)} + Y_{inter}(t_0, f) \tag{37}$$

where

$$Y_{inter}(t_0, f) = \sigma_v \sum_{\substack{u=-\infty \\ u \neq 0}}^{\infty} \sum_{\substack{l=-\infty \\ l \neq 0}}^{\infty} C_{lu}(\lambda_c, m_r, m_h)\delta(f - lf_h - uf_r) \tag{38}$$

The Y_{inter} is an intermodulation model caused by heartbeat and respiratory signals, where C_{lu} is denoted in (17). The null-point value of Y_{inter} occurs every quarter of the wavelength that is a point in which the quantity is zero; to avoid this, methods based on IQ detection, demodulation and antenna diversity have been proposed. The methods based on IQ demodulation were applied for accurately detecting low signal-to-noise ratio [30] and have the problem of unbalance between IQ channels, but theoretically, there is not intermodulation because it detects the phase.

The proposed model (37) in the neglected intermodulation case is compared with the MATLAB simulation as shown in Figure 4, where the related parameters are referred from Table 1. Respiration and

heartbeat movement amplitudes are given as 1.8 and 0.08 mm, respectively, for a relaxed human [8], and the central frequency is done with 6 GHz following the FCC mask.
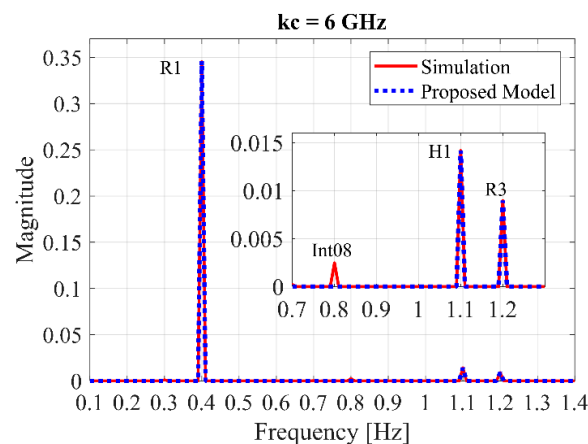
Figure 4. Comparison between the proposed and conventional models. (Insets: zoom in on H_1 and R_3 with scope 0.7–1.3 Hz).

Table 1. Simulation parameters [1].

Parameters	Quantity	Value
d_0	nominal distance	1 m
σ_v	reflection amplitude	1
m_h	heartbeat amplitude	0.08 mm
f_h	heartbeat frequency	1.1 Hz (66 beats/min)
m_r	respiratory amplitude	1.8 mm
f_r	respiratory frequency	0.4 Hz (24 beats/min)
A_0	Tx voltage	1 V
k_c	central frequency	6 GHz (follow FCC)
f_{s_fast}	sampling frequency in fast time	1000 GHz (for comparing to theory)
PRI	pulse repetition interval	25 ns
τ_{max}	maximum slow time	100 s
f_{s_slow}	sampling frequency in slow time	200 Hz

[1] Note all simulations are done with Intel Core i7-3770 CPU of 3.4 GHz, RAM 8 GB, 64-bit, Windows 8.1 Pro, and MATLAB 2018a.

As illustrated in Figure 4, the result from the proposed model is in good agreement with that of the simulation, while the proposed model is faster than computing the simulation. The intermodulation effect (Int08) and third respiratory harmonic (R_3) occur at 0.8 and 1.2 Hz, respectively, and they are strongly dependent on the respiratory movements (chest motions). The third respiratory harmonic is a serious problem that is often close to the heartbeat frequency H_1 [25], in this case, H_1 is at 1.1 Hz. However, these interferences could be filtered out, as suggested in [25], or trying to find a best orientation, as proposed in [42].

4. Analysis of Optimal Central Frequency

In the following section, numerical simulations are performed to verify the performance of the new formula and optimal frequency.

4.1. Detected Respiratory Strength

The study of frequency response of the respiratory model (21) is shown in Figure 5. Figure 5a illustrates the value of R_1 (dB) versus the central frequency with m_r varying from 0.8 to 12 mm while m_h is assumed to be fixed at 0.08 mm, which is typical in ordinary people [8]. The other parameters are fixed, as shown in Table 1. Figure 5b shows the plot of optimal central frequency versus respiratory amplitude m_r with m_h varying from 0.02 to 0.2 mm.
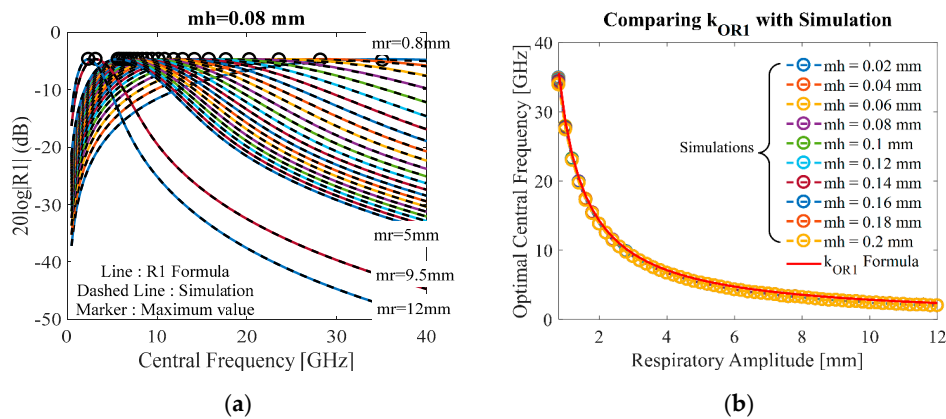
Figure 5. (**a**) Comparison between R_1 model and simulation with small-large respiratory amplitudes m_r = 0.8–12 mm at the assumed heartbeat m_h = 0.08 mm; (**b**) comparison between k_{OR1} formula and simulation with varying heartbeat amplitude m_h = 0.02–0.2 mm.

From Figure 5a, the curve graph described the tendency to respond at greater respiratory amplitude m_r when the central frequency starts to match the system's natural frequency (its resonant frequency) of the periodically chest vibration. It is seen that, for each m_r, as the central frequency increases, the value of R_1 increases and reaches the highest value (optimal), and then starts to decline. For large values of m_r, the value of R_1 increases to the highest point and declines more quickly than those with smaller m_r. This can be explained as follows: the larger value of m_r increases the speed of $J_u(4\pi m_r/\lambda)$. The plot of the simulated optimal frequency versus the respiratory amplitude m_r is shown in Figure 5b compared to the simple formula k_{OR1} in (25). The results show that the k_{OR1} formula (solid line) is almost identical to the simulation results (marker), which remains almost unchanged over the varying the heartbeat amplitude m_h. This means that the optimal frequency is strongly dependent on the respiratory amplitude m_r. Also, when the respiratory amplitude becomes large, the optimal frequency for the maximization decreases.

4.2. Detected Heartbeat Strength

Following the same suggestions in Figure 5, the accuracy of the heartbeat model (28) is also compared with the simulation versus the central frequency as shown in Figure 6a.
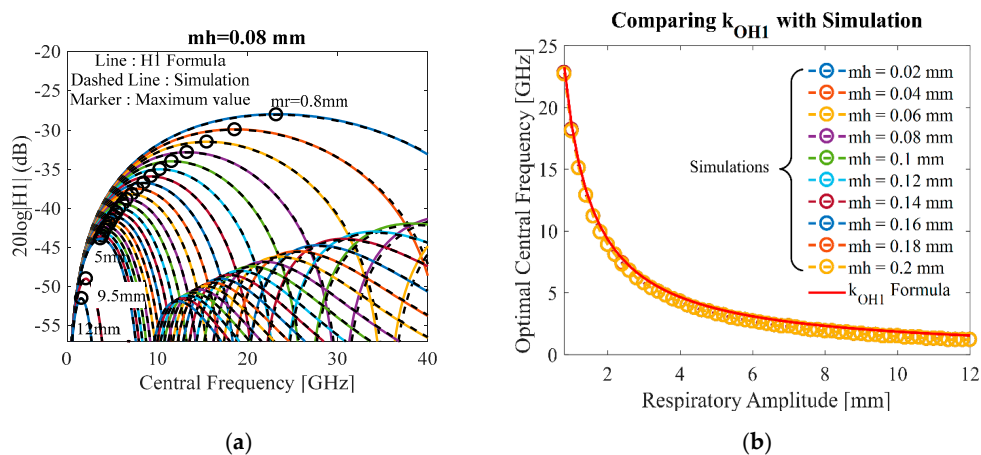
Figure 6. (**a**) Comparison between H_1 formula and simulation with small–large respiratory amplitudes m_r = 0.8–12 mm at the assumed heartbeat m_h = 0.08 mm; (**b**) comparison between k_{OR1} formula and simulation with varying heartbeat amplitude m_h = 0.02–0.2 mm.

As shown in Figure 6a, as the central frequency increases, the heartbeat value H_1 increases until it reaches the maximum value at the optimal central frequency. When the central frequency becomes too high, the strength H_1 starts decreasing, especially for those with large values of m_r. Intuitively, if the respiratory amplitude m_r becomes large, it causes the H_1 peak to drop quickly. This is because the chest surface vibration interferes directly with the heartbeat motion corresponding to the H_1 function in (28). This means that the strength H_1 depends on m_h and especially m_r.

The optimal frequency simulations in Figure 6a are compared with the simple Equation (33) as shown in Figure 6b with the same conditions as Figure 5b. The optimal central frequency begins to reduce when the respiratory amplitude becomes large. The simulation results are almost unchanged with the heartbeat amplitude m_h, this means that the optimal frequency value is strongly dependent on the respiratory amplitude m_r.

4.2.1. Comparison of Heartbeat Strength with R_3 Harmonic

According to Figure 4, the H_1 spectrum tends to be associated directly to the third respiration harmonic (R_3). In order to improve the H_1 strength, the relative strength H_1/R_3 must be considered as in Figure 7a. It is shown that as the central frequency increases, the relative strength decreases, but not cause $H_1/R_3 \leq 1$ for the detectable H_1 spectrum [8].

(a)   **(b)**
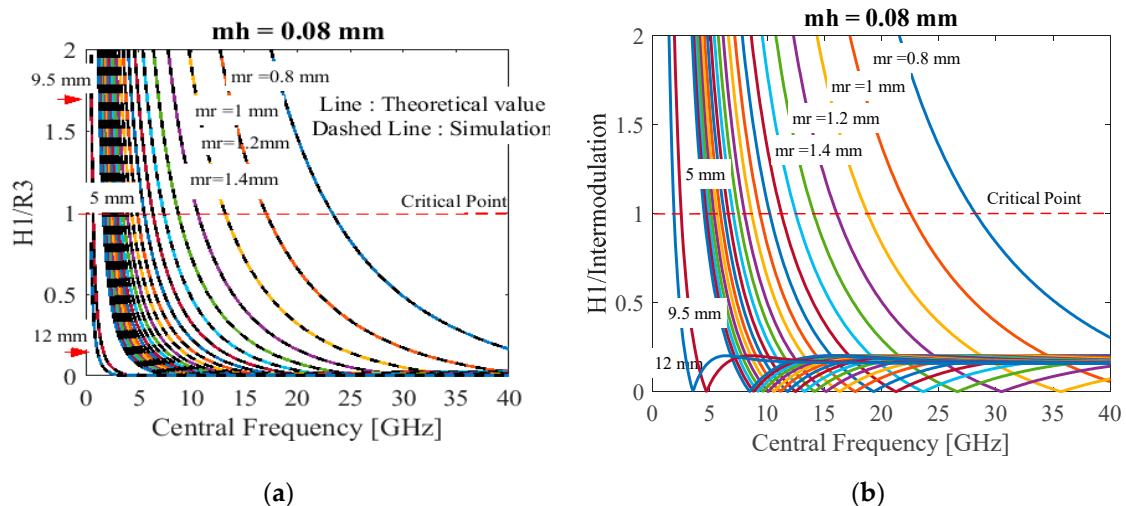
Figure 7. The relative strength versus the central frequency with the small–large respiration amplitudes m_r from 0.8 to 12 mm at the heartbeat m_h of 0.08 mm: (**a**) H_1/R_3; (**b**) $H_1/$Int08.

4.2.2. Comparison of Heartbeat Strength with Intermodulation

The H_1 strength is compared with the intermodulation effect (Int08) at 0.8 Hz according to Figure 4, resulting in Figure 7b with the same suggestions in Figure 5. The relative strength $H_1/$Int08 decreases when the central frequency becomes high, but also not causing $H_1/$Int08 ≤ 1 [8].

According to Figure 7a,b, the R_3 effect is more serious than the intermodulation, because R_3 is very close to H_1 and the highest peak of the harmonics. Therefore, the H_1 signal can be maximized in the premise that the R_3 harmonic is not so large as to affect the detection accuracy [8]. In addition, a best strategy could be to filter these harmonics and interferences, as suggested in [25], or trying to find a best orientation, as proposed in [42].

4.3. Discussion on the Optimal Central Frequency

We consider the behaviors R_1, H_1, $H_1/$Int08, and R_1/R_3 versus the same frequency as shown in Figure 8 with the respiration and heartbeat amplitudes of 1.8 and 0.08 mm, respectively, which are the typical values of a relaxed human [8]. Figure 8a shows a graph of R_1 and H_1 magnitudes and the relative strength of H_1/R_3, $H_1/$Int08, R_1/R_3 are analyzed in Figure 8b.
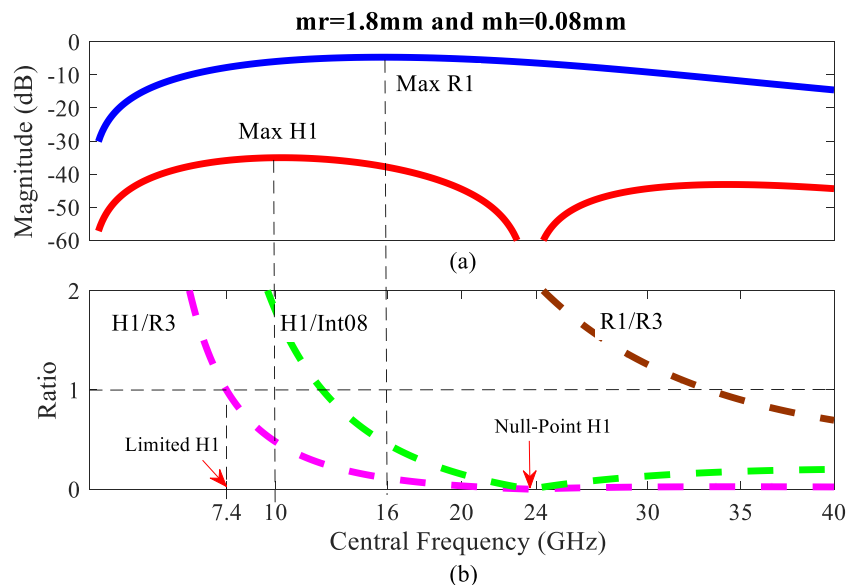
Figure 8. Sequencing the central frequency: (**a**) R_1 and H_1 magnitudes (dB); (**b**) the relative strengths of H_1/R_3, $H_1/Int08$, and R_1/R_3.

For improving the H_1 strength with the condition of $H_1/R_3 > 1$, its optimal frequency has the lowest value shown in Figure 8b; in this case, it should not exceed 7.4 GHz. The R_3 harmonic can be removed, and the frequency can be increased up to the maximum H_1 at 10 GHz computed from (33), corresponding to Figure 8a. In addition, we can avoid the null-point H_1 from evaluating (36). In this case, calculating the null-point frequency is approximately 24 GHz, corresponding to Figure 8b. Using through-the-wall radar, the respiratory signal could be enough to detect life, and also maximized using the optimal central frequency computed from the simple Equation (25). In this case, calculating the optimal frequency is about 16 GHz, corresponding to Figure 8a.

Finally, Figure 8 shows that the central frequency should be limited to the lower region of the *Ka*-band for typical values of human chest wall movement [8].

4.4. Comparison between UWB and CW Radars

In [8], the received baseband signal of CW radars for the vital sign signal can be approximated as

$$B(\tau) = B_0 \cos\left[\frac{4\pi d(\tau)}{\lambda} + \theta\right] \tag{39}$$

Determining the amplitude, B_0 is assumed as 1, the distance $d(\tau)$ is denoted in (6), the total phase shift θ is assumed as 90°, the wavelength λ is demonstrated from $f = 500$ MHz to 40 GHz, and the related parameters are referred from Table 1. The CW carrier frequency is compared with the UWB center frequency for the analysis of the behaviors R_1, H_1, H_1/R_3, and $H_1/I08$, as shown in Figure 9, with the relaxed respiration $m_r = 0.8$–3 mm and heartbeat $m_h = 0.08$ mm [8,23–26,28]. Note that the CW simulation results using the MATLAB program are equal to the ADS results in [8].

As illustrated in Figure 9a, the UWB radar can detect the respiratory strength better than CW at the same frequency; this does not apply at the higher frequency. Unfortunately, from Figure 9d, the relative strength H_1/R_3 of UWB is less than CW at the same frequency, which means the CW radar is more efficient than UWB for detecting the heartbeat signal at the same frequency. Further, from Figure 9b, both UWB and CW radars find it difficult to detect the heartbeat signal using a lower frequency < 1 GHz.

(**a**)

(**b**)

(**c**)

(**d**)
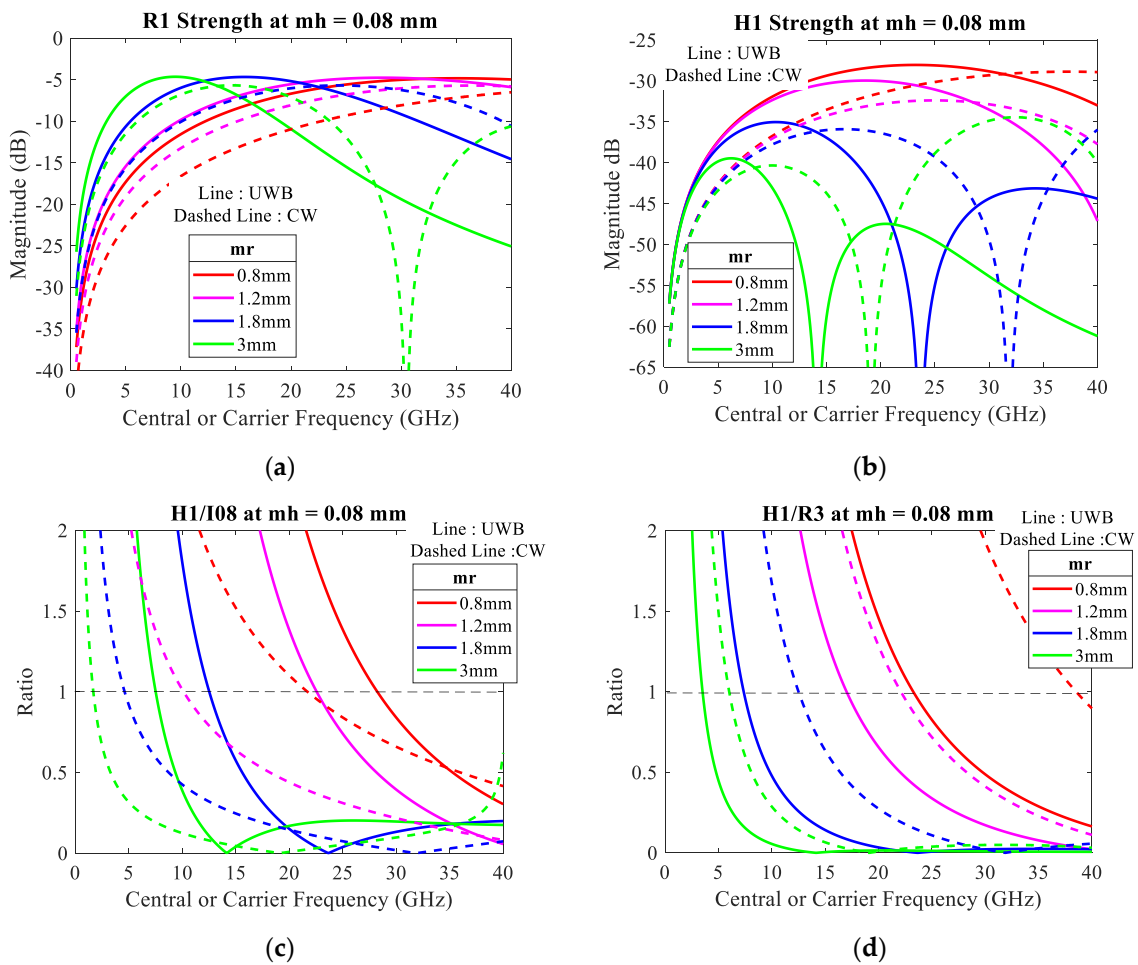
Figure 9. Comparison between ultra-wide band (UWB) central frequency (line) and continuous wave (CW) carrier frequency (dashed line) with respiratory amplitudes mr = 0.8–3 mm at heartbeat amplitude mh = 0.08 mm: (**a**) respiratory strength; (**b**) heartbeat strength; (**c**) the relative strength of heartbeat compared with intermodulation effect of 0.8 Hz; (**d**) the relative strength of heartbeat compared with 3rd respiratory harmonic.

5. Experimentation for Optimal Central Frequency of Respiration

The UWB radar system used for this experiment is shown in Figure 10. The experimental components are listed in Table 2.
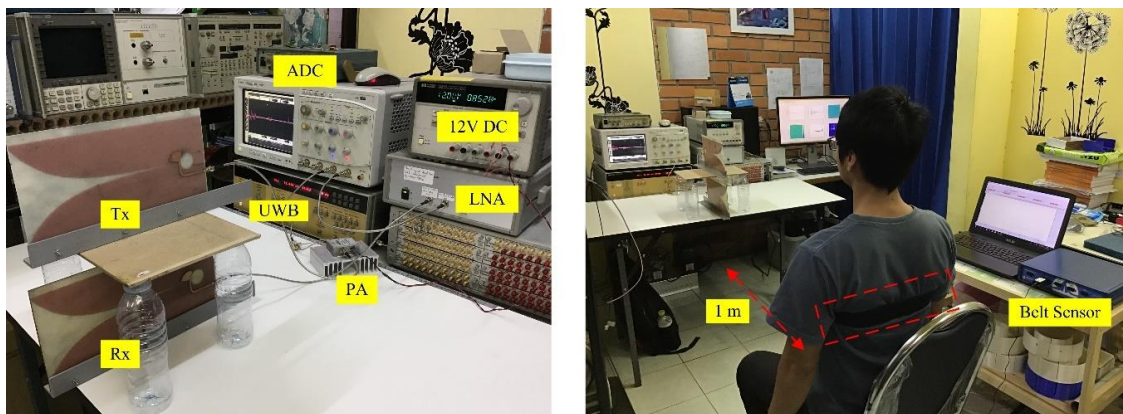
Figure 10. Experimental setup with a human range of 1m according to block diagram in Figure 2a.

Table 2. Equipment List.

Block	Manufacturer	Specifications
UWB source	HP-8133A pulse generator	0.5 V Peak voltage, Central frequency 3 GHz,
Tx and Rx antennas	Vivaldi type (S-band)	2–5 GHz, 10 dBi Angular width (3 dB) $\approx$ 45°
PA	ZVE-8G + Mini-Circuits	2–8 GHz, 30 dBm
LNA	R&K-AA260-OS	2–5 GHz, 26 dBm
ADC	Agilent Oscilloscope, Infiniium DSO80604B	Max frequency 6 GHz Sampling rate 40 GSa/s
USB port	Agilent GPIB, 82357B	Transfer over 850 KB/sec
Belt sensor	BIOPAC Systems	Records respiratory effort
Transmission Power	-	−5 dBm, bandwidth of 2–5 GHz

Before the actual experiment, the preliminary step was done by measuring the respiratory signal of a person sitting 1 m from the UWB radar, as shown in Figure 10. A belt sensor was used to measure the person's respiratory movement amplitude and the result is shown in Figure 11a,b. As shown in Figure 11a, the peak value m_r of the sinusoidal waveform is not constant over the time of measurement. In practice, this alteration is always the case and should be expected to be seen, although the person is sitting still. From the belt measurement, the average value of m_r is approximately 9.5 mm. As shown in Figure 11b, the frequency domain shows two dominant spectra at 0.38 and 0.42 Hz, which correspond to respiratory rates of 22.8–25.2 breaths per minute. To measure the respiration signal, a monocycle waveform was generated by the UWB source with the 3-GHz central frequency and time duration $t_d = 0.1$ ns computed by $t_d = 1/(\pi k_c)$. The measurements of the transmitted waveform by the oscilloscope and corresponding frequency domain are shown in Figure 12a.
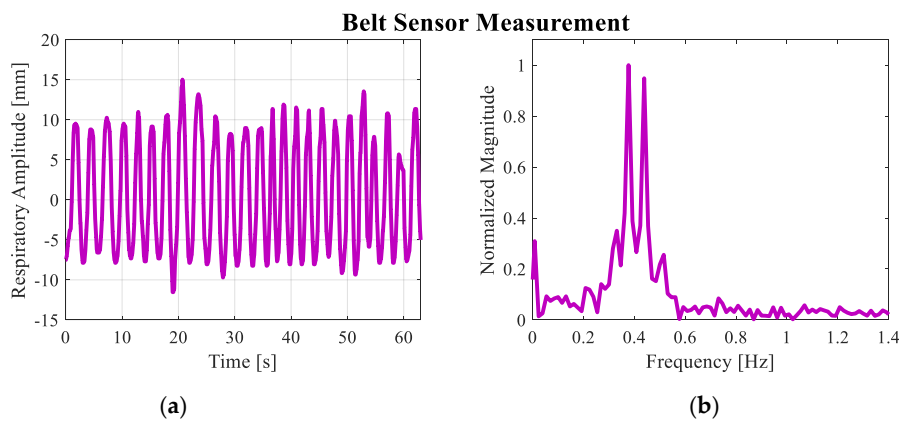
Figure 11. The respiratory movement amplitude measured by a belt sensor; (**a**) time domain; (**b**) frequency domain.

In this system, the peak transmitted power is about −5 dBm and the operable frequency is from 2 to 5 GHz for all components. The system bandwidth does not fully follow the FCC regulations of 3.1–10.6 GHz, which is set to limit interference to existing communication systems only, but in this experiment the power on the chest surface does not exceed 10 W/m^2 (permissible exposure limit), thus the electromagnetic radiation poses no safety threat [43]. The received reflected signal from the human subject was amplified by the LNA and sent to the oscilloscope. The signal on the oscilloscope was captured and transferred to a PC via the GPIB port interface and then the data were discretized by MATLAB program for further signal processing. The slow-time signals were captured approximately at the rate of 512 times in 80 s. For each slow-time measurement, the received signals were measured over the duration of 25 ns (fast time), which is then discretized to 7985 points. Figure 12b shows the received signals measured in fast-time domain with multiple overlapping slow-time measurements.

Figure 12c shows the corresponding 2D-matrix (7985 × 512) of fast-time versus slow-time plots. The antenna coupling as well as the signal-to-noise ratio (SNR) can be improved by using basic filters to remove static signals, like linear least-squares, smooth filter, and bandpass filter for slow and fast-time domains [22,31,44]. The fast Fourier transform (FFT) technique was used to compute the Doppler shift of the vital sign signals [22–39]. The plots of Doppler shift are shown in Figure 13a where the theory plot has been compared with experimental UWB measurement. In this case, the plots show no intermodulation between heartbeat and respiration, due to the use of 3-GHz central frequency which is too low.

(a)   (b)   (c)
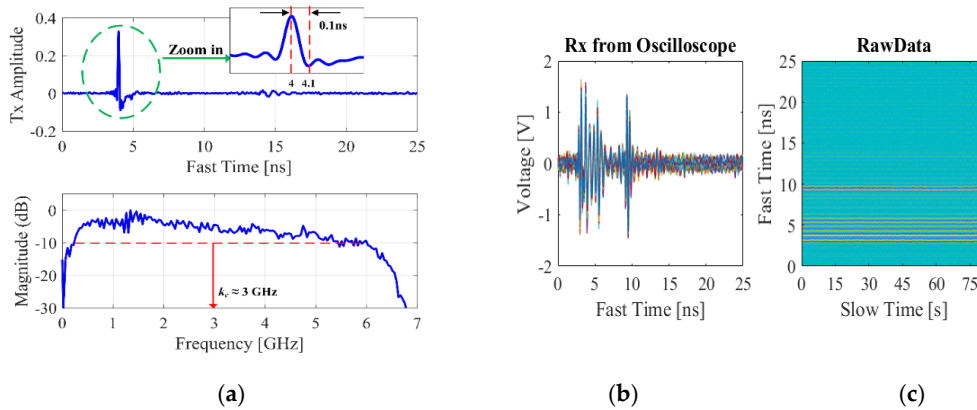
Figure 12. (**a**) The mono-pulse wave form with t_d 0.1ns and 3-GHz central frequency; (**b**) the multiple Rx signals; (**c**) the 2D matrix of the Rx signal data.

(a)   (b)

(c)   (d)
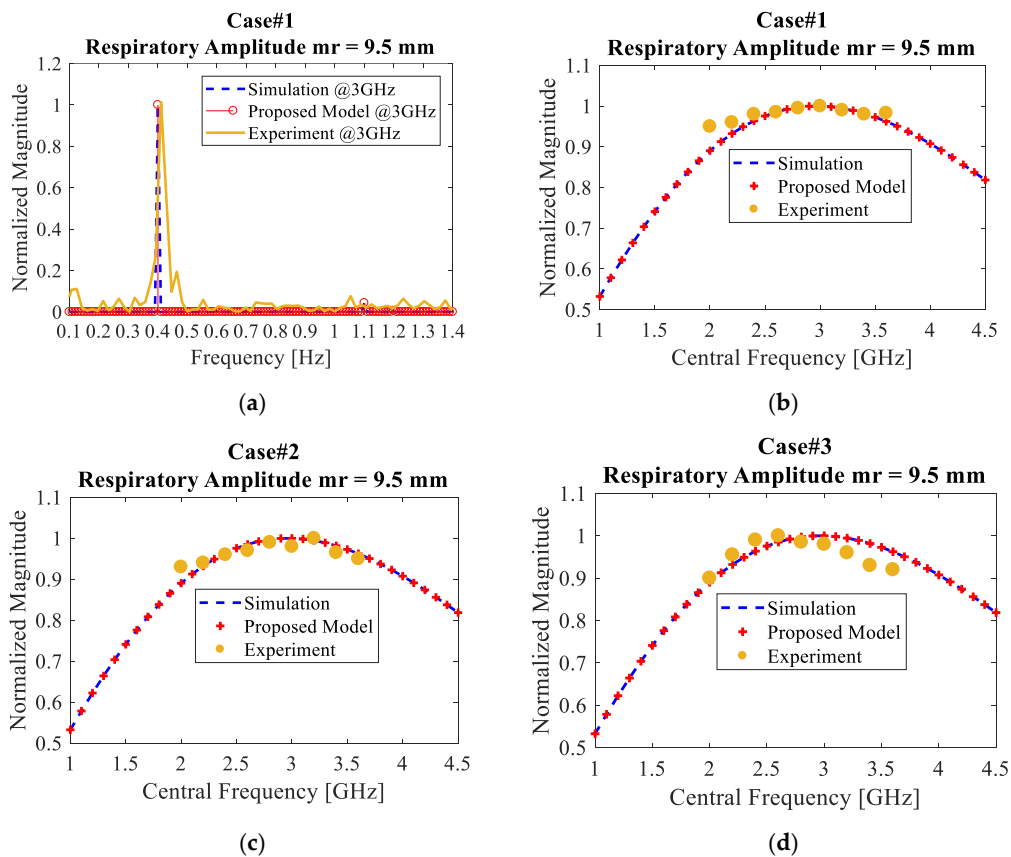
Figure 13. (**a**) The results of the experiment, proposed model, and simulation at 3 GHz central frequency for case#1; the respiration strength versus the central frequency for case #1, case #2 and case #3 shown in (**b–d**), respectively.

Next, the main experiments were carried out to investigate the frequency characteristic of the received signal magnitude. The received signal measurements were taken with three trials, with three different persons, and the central frequency of the transmitted signal was varied from 2 to 4 GHz. As shown in Figure 13b–d, the measurement results of the three cases are compared with the theory plot where m_r is assumed to be 9.5 mm and the optimal central frequency is calculated by the proposed Equation (25) to be 3 GHz.

From Figure 13b,c, it is probably difficult to see that the maximum magnitudes do occur at 3.0 and 3.1 GHz, respectively, because the experimental curves are almost flat. However, as shown in Figure 13d, it is obvious to see the optimal frequency characteristic where the normalized magnitude of the received signal is increased from 0.9 (at 2.0 GHz) to maximum 1.0 (at 2.6 GHz) and then starts to decline at the higher central frequencies. The mismatches between the theory plots and experimental plots are mostly due to the fact that the amplitude of chest movement in practice is not periodic over the time. As opposed to (6), which assumes m_r to be constant, the amplitude of human chest movement does not follow perfect sinusoidal form, as measured and shown in Figure 11a. Another reason could be the loss of symmetry of the monocycle pulse that normally comes from the limited bandwidth of the antennas and other RF components, which is very typical in the real-world situations [44].

The experiment was not carried out to measure the heartbeat signals due to testing the large respiratory amplitude movement (m_r = 9.5 mm) and the lack of higher frequency capabilities of our hardware, these results correspond to the heartbeat strength analysis in Figure 6a. To see the better optimal frequency characteristic of the vital-sign signal strength, a wider range of frequencies for the experimental part may be suitable for future study.

6. Conclusions

The detection of vital signs using radar system is essentially based on interpreting the echo signals scattered from human micromovements. These vital movements induce changes in frequency, amplitude and time-of-arrival of the received signals. Monocycle UWB radar is popularly used as a non-contact monitor since it could free the person from wearable sensors and imposes no infringement on personal privacy. However, due to the distance between the target and the radar, the stronger received signal is strictly required to overcome noises and interferences, especially for tiny vital motions such as breathing and heartbeat motions. In this paper, it was shown that, while other parameters were kept as constants, the magnitudes of the heartbeat and breathing signals could be improved by adjusting the central frequency of the transmitted monocycle waveform.

In this study, the formula for optimal central frequency had been derived and presented, based on the calculus derivative-optimization method. Note that, due to the greater intensity of breathing motions, it is easier to detect respiratory movement than heartbeat. For the respiratory detection, the frequency obtained from the proposed formula could be directly applied. However, the heartbeat signal is so weak and is always covered by the larger respiratory signal. Therefore, in order to obtain the optimal central frequency for the heartbeat signal, the proposed formula must be used in conjunction with the minimization of the third harmonic of the respiration signal.

The experimental results and formula are quite different because of the loss of symmetry of the monocycle pulse that normally comes from bandwidth antennas, hardware, environment, etc., in the real-world applications. However, the proposed formula to compute optimal central frequency can be useful in estimating the range of frequencies at which the remote-sensing hardware operates. According to Figures 5a, 6a and 7a, the optimal frequency is higher for smaller respiratory movement m_r. To avoid significant performance deterioration as m_r increases, we could estimate for optimizing the central frequency that should be limited to the lower region of the Ka-band.

Furthermore, as an extra study, we compared the performances of UWB and CW radars. According to simulation results, for given frequencies, the UWB radar is better off at detecting the respiratory signal, while the CW radar performs very well in detecting small signals from heartbeat

motion. For frequencies lower than 1 GHz, both uses of UWB and CW radars find it difficult to detect a small heartbeat signal.

Lastly, it is worth pointing out that this study was done without considering the problems of sampling rates of both fast-time and slow-time domains. Also, the proposed analytical framework was based on the approximation of the Bessel function which was accurate for the heartbeat no greater than 0.3 mm. The aforementioned issues will be revisited and improved in future studies.

Author Contributions: Conceptualization, A.R.; methodology, A.R., P.P. and T.O.; validation, A.R., P.P. and T.O.; formal analysis, A.R., P.P. and T.O.; investigation, A.R., P.P. and T.O.; writing-original draft preparation, A.R.; writing-review and editing, A.R., P.P. and T.O.; and funding acquisition, P.P. All authors have read and agreed to the published version of the manuscript.

Conflicts of Interest: The authors declare no conflict of interest.

References

1. Ren, L.; Kong, L.; Foroughian, F.; Wang, H.; Theilmann, P.; Fathy, A.E. Comparison Study of Noncontact Vital Signs Detection Using a Doppler Stepped-Frequency Continuous-Wave Radar and Camera-Based Imaging Photoplethysmography. *IEEE Trans. Microw. Theory Tech.* **2017**, *65*, 3519–3529. [CrossRef]
2. Muñoz-Ferreras, J.; Peng, Z.; Gómez-García, R.; Li, C. Review on Advanced Short-Range Multimode Continuous-Wave Radar Architectures for Healthcare Applications. *IEEE J. Electromagn. RF Microw. Med. Biol.* **2017**, *1*, 14–25. [CrossRef]
3. Nahar, S.; Phan, T.; Quaiyum, F.; Ren, L.; Fathy, A.E.; Kilic, O. An Electromagnetic Model of Human Vital Signs Detection and Its Experimental Validation. *IEEE J. Emerg. Sel. Top. Circuits Syst.* **2018**, *8*, 338–349. [CrossRef]
4. Lin, F.; Zhuang, Y.; Song, C.; Wang, A.; Li, Y.; Gu, C.; Li, C.; Xu, W. SleepSense: A Noncontact and Cost-Effective Sleep Monitoring System. *IEEE Trans. Biomed. Circuits Syst.* **2017**, *11*, 189–202. [CrossRef] [PubMed]
5. Li, C.; Lubecke, V.M.; Boric-Lubecke, O.; Lin, J. A Review on Recent Advances in Doppler Radar Sensors for Noncontact Healthcare Monitoring. *IEEE Trans. Microw. Theory Tech.* **2013**, *61*, 2046–2060. [CrossRef]
6. Zhao, H.; Hong, H.; Miao, D.; Li, Y.; Zhang, H.; Zhang, Y.; Li, C.; Zhu, X. A Noncontact Breathing Disorder Recognition System Using 2.4-GHz Digital-IF Doppler Radar. *IEEE J. Biomed. Health Inform.* **2019**, *23*, 208–217. [CrossRef]
7. Li, C.; Xiao, Y.; Lin, J. Experiment and Spectral Analysis of a Low-Power Ka-Band Heartbeat Detector Measuring from Four Sides of a Human Body. *IEEE Trans. Microw. Theory Tech.* **2006**, *54*, 4464–4471. [CrossRef]
8. Li, C.; Lin, J. Optimal Carrier Frequency of Non-contact Vital Sign Detectors. In Proceedings of the 2007 IEEE Radio and Wireless Symposium, Long Beach, CA, USA, 7–12 January 2007; pp. 281–284.
9. Anghel, A.; Vasile, G.; Cacoveanu, R.; Ioana, C.; Ciochina, S. Short-Range Wideband FMCW Radar for Millimetric Displacement Measurements. *IEEE Trans. Geosci. Remote Sens.* **2014**, *52*, 5633–5642. [CrossRef]
10. Pfeffer, C.; Feger, R.; Wagner, C.; Stelzer, A. FMCW MIMO Radar System for Frequency-Division Multiple TX-Beamforming. *IEEE Trans. Microw. Theory Tech.* **2013**, *61*, 4262–4274. [CrossRef]
11. Ash, M.; Ritchie, M.; Chetty, K.; Brennan, P.V. A New Multistatic FMCW Radar Architecture by Over-the-Air Deramping. *IEEE Sens. J.* **2015**, *15*, 7045–7053. [CrossRef]
12. Khan, F.; Ghaffar, A.; Khan, N.; Cho, S.H. An Overview of Signal Processing Techniques for Remote Health Monitoring Using Impulse Radio UWB Transceiver. *Sensors* **2020**, *20*, 2479. [CrossRef]
13. Tantiparimongkol, L.; Phasukkit, P. Experiment of UWB Pulse Generator using FPGA based on Delay Line-Based Pulse Generation for Radar Application. In Proceedings of the 2018 International Symposium on Multimedia and Communication Technology (ISMAC 2018), Tottori, Japan, 29–31 August 2018.

14.　Bolea, M.; Mora, J.; Ortega, B.; Capmany, J. Flexible Monocycle UWB Generation for Reconfigurable Access Networks. *IEEE Photonics Technol. Lett.* **2010**, *22*, 878–880. [CrossRef]

15.　Li, J.; Liang, Y.; Wong, K.K. Millimeter-Wave UWB Signal Generation via Frequency Up-Conversion Using Fiber Optical Parametric Amplifier. *IEEE Photonics Technol. Lett.* **2009**, *21*, 1172–1174.

16.　Han, J.; Nguyen, C. A new ultra-wideband, ultra-short monocycle pulse generator with reduced ringing. *IEEE Microw. Wirel. Compon. Lett.* **2002**, *12*, 206–208.

17.　Hsieh, C.; Chiu, Y.; Shen, Y.; Chu, T.; Huang, Y. A UWB Radar Signal Processing Platform for Real-Time Human Respiratory Feature Extraction Based on Four-Segment Linear Waveform Model. *IEEE Trans. Biomed. Circuits Syst.* **2016**, *10*, 219–230. [CrossRef]

18.　Strackx, M.; Faes, B.; D'Agostino, E.; Leroux, P.; Reynaert, P. FPGA based flexible UWB pulse transmitter using EM subtraction. *Electron. Lett.* **2013**, *49*, 1243–1244. [CrossRef]

19.　Zhang, F.; Fu, S.; Wu, J.; Ngo, N.Q.; Xu, K.; Li, Y.; Hong, X.; Shum, P.; Lin, J. UWB Impulse Radio Transmitter Using an Electrooptic Phase Modulator Together with a Delay Interferometer. *IEEE Photonics Technol. Lett.* **2010**, *22*, 1479–1481. [CrossRef]

20.　Chen, X.; Kiaei, S. Monocycle shapes for ultra wideband system. In Proceedings of the 2002 IEEE International Symposium on Circuits and Systems (ISCAS), Phoenix-Scottsdale, AZ, USA, 26–29 May 2002.

21.　Zhang, J.; Abhayapala, T.D.; Kennedy, R.A. Role of pulses in ultra wideband systems. In Proceedings of the 2005 IEEE International Conference on Ultra-Wideband, Zurich, Switzerland, 5–8 September 2005; pp. 565–570.

22.　Rittiplang, A.; Phasukkit, P. UWB Radar for Multiple Human Detection Through the Wall Based on Doppler Frequency and Variance Statistic. In Proceedings of the 2019 12th Biomedical Engineering International Conference (BMEiCON), Ubon Ratchathani, Thailand, 19–22 November 2019; pp. 1–5.

23.　Baldi, M.; Chiaraluce, F.; Zanaj, B.; Moretti, M. Analysis and simulation of algorithms for vital signs detection using UWB radars. In Proceedings of the 2011 IEEE International Conference on Ultra-Wideband (ICUWB), Bologna, Italy, 14–16 September 2011; pp. 341–345.

24.　Lazaro, A.; Girbau, D.; Villarino, R.; Ramos, A. Vital signs monitoring using impulse based UWB signal. In Proceedings of the 2011 41st European Microwave Conference, Manchester, UK, 10–13 October 2011; pp. 135–138.

25.　Lazaro, A.; Girbau, D.; Villarino, R. Analysis of Vital Signs Monitoring Using an IR-UWB Radar. *Prog. Electromagn. Res.* **2010**, *100*, 265–284. [CrossRef]

26.　Rong, Y.; Bliss, D.W. Remote Sensing for Vital Information Based on Spectral-Domain Harmonic Signatures. *IEEE Trans. Aerosp. Electron. Syst.* **2019**, *55*, 3454–3465. [CrossRef]

27.　Mabrouk, M.; Rajan, S.; Bolic, M.; Batkin, I.; Dajani, H.R.; Groza, V.Z. Model of human breathing reflected signal received by PN-UWB radar. In Proceedings of the 2014 36th Annual International Conference of the IEEE Engineering in Medicine and Biology Society, Chicago, IL, USA, 26–30 August 2014; pp. 4559–4562.

28.　Rong, Y.; Bliss, D.W. Direct RF Signal Processing for Heart-Rate Monitoring Using UWB Impulse Radar. In Proceedings of the 2018 52nd Asilomar Conference on Signals, Systems, and Computers, Pacific Grove, CA, USA, 28–31 October 2018; pp. 1215–1219.

29.　Venkatesh, S.; Anderson, C.R.; Rivera, N.V.; Buehrer, R.M. Implementation and analysis of respiration-rate estimation using impulse-based UWB. In Proceedings of the MILCOM 2005—2005 IEEE Military Communications Conference, Atlantic City, NJ, USA, 17–20 October 2005; Volume 5, pp. 3314–3320.

30.　Ren, L.; Wang, H.; Naishadham, K.; Kilic, O.; Fathy, A.E. Phase-Based Methods for Heart Rate Detection Using UWB Impulse Doppler Radar. *IEEE Trans. Microw. Theory Tech.* **2016**, *64*, 3319–3331. [CrossRef]

31.　Liang, X.; Zhang, H.; Fang, G.; Ye, S.; Gulliver, T.A. An Improved Algorithm for Through-Wall Target Detection Using Ultra-Wideband Impulse Radar. *IEEE Access* **2017**, *5*, 22101–22118. [CrossRef]

32.　Ren, L.; Koo, Y.S.; Wang, H.; Wang, Y.; Liu, Q.; Fathy, A.E. Noncontact Multiple Heartbeats Detection and Subject Localization Using UWB Impulse Doppler Radar. *IEEE Microw. Wirel. Compon. Lett.* **2015**, *25*, 690–692. [CrossRef]

33.　Xu, Y.; Dai, S.; Wu, S.; Chen, J.; Fang, G. Vital Sign Detection Method Based on Multiple Higher Order Cumulant for Ultrawideband Radar. *IEEE Trans. Geosci. Remote Sens.* **2012**, *50*, 1254–1265. [CrossRef]

34.　Huang, X.; Sun, L.; Tian, T.; Huang, Z.; Clancy, E. Real-time non-contact infant respiratory monitoring using UWB radar. In Proceedings of the 2015 IEEE 16th International Conference on Communication Technology (ICCT), Hangzhou, China, 18–21 October 2015; pp. 493–496.

35. Xu, Y.; Chen, J.; Dai, S.; Fang, G. Experimental Study of UWB Pulse Radar for Life Detection. In Proceedings of the 2011 1st International Conference on Instrumentation, Measurement, Computer, Communication and Control, Beijing, China, 21–23 October 2011; pp. 729–732.

36. Naishadham, K.; Piou, J.E.; Ren, L.; Fathy, A.E. Estimation of Cardiopulmonary Parameters from Ultra Wideband Radar Measurements Using the State Space Method. *IEEE Trans. Biomed. Circuits Syst.* **2016**, *10*, 1037–1046. [CrossRef]

37. Eren, C.; Karamzadeh, S.; Kartal, M. The artifacts of human physical motions on vital signs monitoring. In Proceedings of the 2019 Scientific Meeting on Electrical-Electronics & Biomedical Engineering and Computer Science (EBBT), Istanbul, Turkey, 24–26 April 2019; pp. 1–5.

38. Liang, X.; Deng, J.; Zhang, H.; Gulliver, T.A. Ultra-Wideband Impulse Radar Through-Wall Detection of Vital Signs. *Sci. Rep.* **2018**, *8*, 13367. [CrossRef]

39. Xikun, H.; Jin, T. Short-Range Vital Signs Sensing Based on EEMD and CWT Using IR-UWB Radar. *Sensors* **2016**, *16*, 2025.

40. Ghufran, S.; Veluvolu, K.C. Surface chest motion decomposition for cardiovascular monitoring. *Sci. Rep.* **2014**, *4*, 5093.

41. Wikipedia contributors, "Gaussian integral," Wikipedia, The Free Encyclopedia. Available online: https://en.wikipedia.org/w/index.php?title=Gaussian_integral&oldid=953684338 (accessed on 20 May 2020).

42. Lazaro, A.; Girbau, D.; Villarino, R. Techniques for Clutter Suppression in the Presence of Body Movements during the Detection of Respiratory Activity through UWB Radars. *Sensors* **2014**, *14*, 2595–2618. [CrossRef]

43. Liang, F.; Qi, F.; An, Q.; Lv, H.; Chen, F.; Li, Z.; Wang, J. Detection of Multiple Stationary Humans Using UWB MIMO Radar. *Sensors* **2016**, *16*, 1922. [CrossRef]

44. Quan, X.; Choi, J.W.; Cho, S.H. A New Thresholding Method for IR-UWB Radar-Based Detection Applications. *Sensors* **2020**, *20*, 2314. [CrossRef]